Theoretical and Computational Aspects of 2-D Inverse Profiling

Anton G. Tijhuis, *Member, IEEE*, Kamal Belkebir, Amélie C. S. Litman, and Bastiaan P. de Hon

***Abstract*—We discuss two techniques for solving two-dimensional (2-D) inverse scattering problems by parameterizing the scattering configuration, and determining the optimum value of the parameters by minimizing a cost function involving the known scattered-field data. The computation of the fields in each estimated configuration is considered as an auxiliary problem. To improve the efficiency of these computations, the CGFFT iterative scheme is combined with a special extrapolation procedure that is valid for problems with a varying physical parameter such as frequency, angle of incidence, or contrast. Further, we analyze the dynamic range and the resolution of linearized schemes. To obtain an acceptable resolution for an object with a large contrast with respect to the surrounding medium, multiple-frequency information is used. Finally, the availability of a fast-forward solver was an incentive to consider nonlinear optimization. In particular, we use a quasi-Newton algorithm at only twice the computational cost of the distorted-wave Born iterative scheme.**

***Index Terms*—Electromagnetic scattering inverse problems, dielectric bodies, imaging, integral equations, iterative methods, permittivity measurement.**

I. Introduction

ALGORITHMS for solving inverse-profiling problems are traditionally expressed as optimization problems in which the unknown configuration is parameterized and the value of the configuration parameters is determined by minimizing some cost function involving the scattered field. This is realized by iterative procedures based on a linearization around a given estimate as well as by nonlinear optimization. Applications to one-dimensional (1-D) inverse-scattering problems have been around for almost three decades. Literature reviews can be found in [1] and [2]. Since 1990, several authors have described generalizations of the 1-D approach to two-dimensional (2-D) configurations [4]–[11].

The main bottleneck solving multidimensional inverse-scattering problems is that *repeated "exact" field computations* require an excessive amount of computation time. This has led to the emergence of modified-gradient methods [12], [13], in which successive approximations of the configuration and the excited fields are obtained simultaneously. These methods have been applied to a range of problems by several authors. A review of this work can be found in [14]. The second important problem is the issue of *convergence*. For linearized methods, convergence is not always guaranteed. Methods based on the optimization of a cost function inherently converge to a minimum, but this may be a local one. One approach that may be effective in avoiding such minima is the quadratic approach suggested in [15], [16].

The work described in the present paper continues the "classical" approach, where the field computation is treated as an auxiliary problem that can be solved efficiently. Results were reported earlier at a number of scientific meetings [17]–[20], but a combination of circumstances has thus far prevented us from writing journal papers. Meanwhile, the research has proceeded, so that we are now able to describe a consistent theoretical analysis and numerical implementation of 2-D inverse profiling problems. The theoretical analysis is not complete but provides enough understanding to devise a systematic and efficient numerical implementation. In our opinion, the understanding that follows from this analysis distinguishes our approach from the "trial and error" on which the development of inverse-scattering schemes is often based.

We first analyze the dynamic range and the resolution of linearized schemes from a theoretical point of view. For the dynamic range, a parameter study is carried out for the special case of homogeneous circular cylinders. For the resolution, we assume that the linearized data equation is exact. Using the linearity, we specialize in the reconstruction of a localized "pixel" that may be considered as a small contrast with respect to a smooth reference medium. The results lead to the conclusion that configurations with a large contrast with respect to the surrounding medium can be reconstructed with an acceptable resolution by using multiple-frequency information. This conclusion was also reached by other authors [22], [23]. A second result from the theoretical analysis is the parameterization of the unknown susceptibility profile. We approximate this profile by piecewise-linear interpolation and remove ambiguities due to local oversampling by adding a regularization term to the cost function. This term restricts the linear variation over adjacent cells and is thus consistent with the parameterization.

A second feature of our implementation is the fast solution of the underlying forward problem, which is achieved by combining the CGFFT method with a special extrapolation procedure. This method is capable of solving a discretized field equation for a varying physical parameter with a numerical effort equivalent to completely solving a few forward problems [24]–[26]. It is this efficiency that has made inversion methods based on exact field computations feasible again, even com-

Manuscript received July 4, 2000; revised March 8, 2001. This work was supported in part by a postdoctoral fund from the Eindhoven University of Technology, Eindhoven, The Netherlands.

A. G. Tijhuis and B. P. de Hon are with the Faculty of Electrical Engineering, Eindhoven University of Technology, Eindhoven, The Netherlands.

K. Belkebir is with the Institut Fresnel, Domaine Universitaire de Saint-Jérome, Marseille Cedex 20, France.

A. C. S. Litman is with Schlumberger Riboud Production Center, Clamart Cedex, France.

Publisher Item Identifier S 0196-2892(01)05109-9.

pared with gradient-type methods. The update step in linearized inversion now typically takes at least as much time as the field computation. This suggests that it should be possible to replace that step by a line search in a nonlinear optimization procedure based entirely on repeated field computations. A discussion of an implementation based on the quasi-Newton method concludes this paper.

We illustrate our approach by a few representative numerical results. For tutorial purposes, we restrict ourselves in these examples to a lossless dielectric object. This allows us to avoid the discussion of the frequency dependence of a complex permittivity. However, all algorithms presented in this paper have been tested successfully for lossy objects and/or lossy surrounding media as well.

II. Formulation of the Problem

In this section, we describe the configuration. Subsequently, some basic relations are given that are needed throughout the text. Finally, we formulate the inverse-scattering problem as an optimization problem for a parameterized configuration.

A. The Configuration

We consider a 2-D inhomogeneous, isotropic dielectric cylinder in a homogeneous surrounding medium. As shown in Fig. 1, the interior of the cylinder is represented as $\mathcal{D}_2$, the boundary as $\partial\mathcal{D}$, and the exterior as $\mathcal{D}_1$. For the permittivity, we have $\varepsilon = \varepsilon_2(\boldsymbol{\rho})$ in $\mathcal{D}_2$ and $\varepsilon = \varepsilon_1$ in $\mathcal{D}_1$, while the permeability $\mu = \mu_0$ in $\mathcal{D}_1 \cup \mathcal{D}_2$. Both $\varepsilon_2(\boldsymbol{\rho})$ and ε_1 may assume complex values. In the direct-scattering problem, both the shape and the constitution of the cylinder are completely known. In the inverse-scattering problem, we assume that the cylinder is enclosed in a square domain of width $2a$ centered around the z-axis. The configuration is excited by an electrically polarized, time-harmonic line source that is located on an observation contour $\partial\mathcal{D}_O$. The electric field is detected by receivers on the same contour. The observation domain $\mathcal{D}_O$ is a region of $\mathbb{R}^2$ bounded by $\partial\mathcal{D}_O$. A time factor of $\exp(st)$ with $s = \beta + j\omega$ is assumed implicitly in all fields and currents mentioned in this paper.

To avoid "inverse crimes," the boundary information is only used in generating the scattered-field data for the exact profile. In the inversion, we only use the information that the object is located in $\mathcal{D}_O$. Since $\mathcal{D}_2 \in \mathcal{D}_O$, we will therefore formulate all integral equations for a contrast in $\mathcal{D}_O$, so that these equations also describe the approximate direct-scattering problems that are solved in each iteration of the inversion.

We consider two choices for the contour $\partial\mathcal{D}_O$. The first choice is a circle with $\rho = \rho_O > a\sqrt{2}$ centered around the z-axis. For this contour, we have the following equivalence theorems.

1) Any incident field in the region $\rho < \rho_O$ can be represented as being generated by a surface current on $\partial\mathcal{D}_O$, embedded in a homogeneous dielectric with the properties of the surrounding medium.
2) Any scattered field in the region $\rho > \rho_O$ can be expressed in terms of the electric field on $\partial\mathcal{D}_O$.

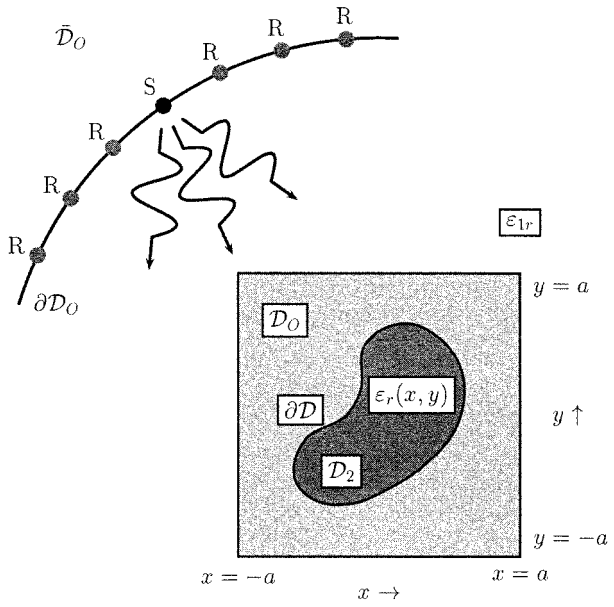

Fig. 1. The dielectric cylinder, part of the observation contour and the various domains mentioned in the text. The region $\mathcal{D}_1$ is the region outside $\partial\mathcal{D}$.

Both theorems are derived in Appendix A. Combining these theorems leads to the conclusion that the scattering behavior of the interior of $\partial\mathcal{D}_O$ is completely characterized by the scattered field at $\boldsymbol{\rho} = \boldsymbol{\rho}_R$ caused by a line source at $\boldsymbol{\rho} = \boldsymbol{\rho}_S$, with $\boldsymbol{\rho}_R$ and $\boldsymbol{\rho}_S$ being arbitrary points on $\partial\mathcal{D}_O$. Hence, no new information can be obtained by exciting the object with other sources in $\rho > \rho_O$ and detecting the scattered field in the same domain.

The second choice for $\partial\mathcal{D}_O$ is a straight line at $y = y_O > a$. For this contour, similar conclusions can be drawn with respect to observation in $y > y_O$. The difference between both choices is observed by considering which plane waves are excited and detected. A single plane wave can be written as

$$E(x, y) = A \exp(-jk_x x - jk_y y) \tag{1}$$

with $k_x = k_1 \cos(\phi_k)$ and $k_y = k_1 \sin(\phi_k)$, with $k_1 = \omega/c_1$. For excitation and detection on a circle, we have $-\pi < \phi_k \leq \pi$ for both the incident and the scattered field. Since these plane waves allow a complete representation of any source-free field in the surrounding medium, we refer to this choice as the case of *complete data*. When $\partial\mathcal{D}_O$ is a straight line, the incident field contains only "downgoing" waves with $\phi_k < 0$. Therefore, we refer to this choice as the case of *partial data*.

In the description of the theoretical results and of the numerical implementation, we concentrate on the case of complete data. However, as demonstrated by the numerical results, most of the analysis can be generalized to the case of partial data.

B. Basic Relations

Since the forward problem is linear, it suffices to consider Green's function, i.e., the solution of the second-order differential equation

$$\left[\nabla_T^2 - \frac{s^2}{c_0^2}\,\varepsilon_r(\boldsymbol{\rho})\right] G(\boldsymbol{\rho}, \boldsymbol{\rho}_P) = -\delta(\boldsymbol{\rho} - \boldsymbol{\rho}_P) \tag{2}$$

that satisfies the radiation condition

$$\lim_{\rho\to\infty}\sqrt{\rho}\left[\partial\rho\, G(\boldsymbol{\rho},\boldsymbol{\rho}_P)+\frac{s}{c_1}G(\boldsymbol{\rho},\boldsymbol{\rho}_P)\right]=0. \tag{3}$$

In (2) and (3), $\boldsymbol{\rho}$ and $\boldsymbol{\rho}_P$ are 2-D position vectors, ∇_T is the 2-D gradient operation, c_0 is the speed of light in free space, c_1 is the complex wave speed in the $\mathcal{D}_1$, ε_r is a complex relative permittivity and $\delta(\boldsymbol{\rho})$ is a 2-D delta function. Equation (2) is valid for all $\boldsymbol{\rho}\in\mathbb{R}^2$, with $\varepsilon_r(\boldsymbol{\rho})=\varepsilon_{1r}$ for $\boldsymbol{\rho}\in\mathcal{D}_1$.

With the aid of the radiation condition (3) and Green's second identity, it can be shown directly that G satisfies the reciprocity relation:

$$G(\boldsymbol{\rho}_P,\boldsymbol{\rho}_Q)=G(\boldsymbol{\rho}_Q,\boldsymbol{\rho}_P) \tag{4}$$

for any pair $\{\boldsymbol{\rho}_P,\boldsymbol{\rho}_Q\}$ in $\mathbb{R}^2$.

Equation (2) can be reduced to an equivalent *integral relation*. We introduce a reference medium with relative permittivity $\overline{\varepsilon}_r(\boldsymbol{\rho})$ and the corresponding Green's function $\overline{G}(\boldsymbol{\rho},\boldsymbol{\rho}_P)$. In principle $\overline{\varepsilon}_r(\boldsymbol{\rho})$ may be chosen arbitrarily; in the present context we will assume that this parameter only differs from ε_{1r} inside $\mathcal{D}_O$. Subtracting the differential equations for G and $\overline{G}$, writing the contrast source as a superposition of delta functions, and using the reciprocity relation (4) for $\overline{G}$ results in the contrast-type integral relation

$$\begin{aligned}&G(\boldsymbol{\rho},\boldsymbol{\rho}_P)-\overline{G}(\boldsymbol{\rho},(\boldsymbol{\rho}_P)\\&\quad=-\frac{s^2}{c_0^2}\iint_{\mathcal{D}_O}\left[\varepsilon_r(\boldsymbol{\rho}')-\overline{\varepsilon}_r(\boldsymbol{\rho}')\right]\overline{G}(\boldsymbol{\rho}',\boldsymbol{\rho})\,G(\boldsymbol{\rho}',\boldsymbol{\rho}_P)\,dA(\boldsymbol{\rho}')\end{aligned} \tag{5}$$

which again holds for any pair $\{\boldsymbol{\rho},\boldsymbol{\rho}_P\}$ in $\mathbb{R}^2$. Equation (5) is the cornerstone of our approach of reconstructing $\varepsilon_r(\boldsymbol{\rho})$.

C. Parameterization and Cost Function

Any computational reconstruction procedure can only yield $\varepsilon_r(\boldsymbol{\rho})$ with limited resolution. In Section IV, it will be argued that, for iterative procedures, this resolution depends on the operating frequency ω and the local average value of ε_r. This means that we have to introduce a parameterization for the unknown profile. For now, it suffices to write the relative permittivity as

$$\tilde{\varepsilon}_r(\boldsymbol{\rho})=\varepsilon_{1r}+\tilde{\chi}(\boldsymbol{\rho})=\varepsilon_{1r}+\sum_\alpha\tilde{\chi}_\alpha\psi_\alpha(\boldsymbol{\rho}) \tag{6}$$

where $\{\psi_\alpha(\boldsymbol{\rho})\}$ is a finite set of known, real-valued expansion functions with support inside the observation domain $\mathcal{D}_O$. The symbol $\tilde{\chi}$ was chosen since, for an object in free space, $\varepsilon_{1r}=1$ and the sum in the right-hand side of (6) is a dielectric susceptibility. The parameters $\{\tilde{\chi}_\alpha\}$ are obtained by minimizing a cost function of the form

$$J(\{\tilde{\chi}_\alpha\})=\int_{-\pi}^{\pi}d\phi_R\int_{-\pi}^{\pi}d\phi_S\left|\tilde{G}(\boldsymbol{\rho}_R,\boldsymbol{\rho}_S)-G(\boldsymbol{\rho}_R,\boldsymbol{\rho}_S)\right|^2 \tag{7}$$

where $G(\boldsymbol{\rho}_R,\boldsymbol{\rho}_S)$ is the known field at receiver position $\boldsymbol{\rho}=\boldsymbol{\rho}_R$ for a source at $\boldsymbol{\rho}=\boldsymbol{\rho}_S$, and $\tilde{G}(\boldsymbol{\rho}_R,\boldsymbol{\rho}_S)$ is the corresponding field in a parameterized configuration. In the actual implementation, which will be discussed in Section V, we augment the cost function (7) by a suitably chosen regularization term to compensate for any possible oversampling in (6). Thus, we have written the problem as an optimization problem for the parameters $\{\tilde{\chi}_\alpha\}$, while the determination of the fields in a parameterized configuration may be envisaged as an auxiliary computation in an "inner loop."

III. Linearized Scheme: Method of Solution

The problem formulated in Section II is inherently nonlinear, since the field inside the observation domain is determined by the unknown permittivity profile. One way to handle this problem is to linearize the equation pertaining to the known scattered field data around the best available estimate. This is known as the distorted-wave Born approximation. By using this approximation repeatedly in an iterative procedure, we are able to reconstruct objects with a larger contrast with respect to the surrounding medium than would be possible with the conventional Born approximation. Both ideas are described in this section.

A. Distorted-Wave Born Approximation

As a first step toward formulating our method of solution, we choose $\overline{\varepsilon}_r(\boldsymbol{\rho})$ in (5) as an estimate of $\varepsilon_r(\boldsymbol{\rho})$. For a field generated by a source at $\boldsymbol{\rho}=\boldsymbol{\rho}_S$ and detected by a receiver at $\boldsymbol{\rho}=\boldsymbol{\rho}_R$, we then have

$$\begin{aligned}&G(\boldsymbol{\rho}_R,\boldsymbol{\rho}_S)-\overline{G}(\boldsymbol{\rho}_R,\boldsymbol{\rho}_S)\\&\quad=-\frac{s^2}{c_0^2}\iint_{\mathcal{D}_O}\left[\varepsilon_r(\boldsymbol{\rho})-\overline{\varepsilon}_r(\boldsymbol{\rho})\right]\overline{G}(\boldsymbol{\rho},\boldsymbol{\rho}_R)G(\boldsymbol{\rho},\boldsymbol{\rho}_S)\,dA(\boldsymbol{\rho}).\end{aligned} \tag{8}$$

The *data equation* (8) is a nonlinear equation for the unknown permittivity profile $\varepsilon_r(\boldsymbol{\rho})$, since G also depends on this profile. To facilitate its solution, we introduce a *linearization* by taking the counterpart of (8) for $\boldsymbol{\rho}\in\mathcal{D}_O$ and $\boldsymbol{\rho}_S\in\partial\mathcal{D}_O$

$$\begin{aligned}G(\boldsymbol{\rho},\boldsymbol{\rho}_S)=&\overline{G}(\boldsymbol{\rho},\boldsymbol{\rho}_S)-\frac{s^2}{c_0^2}\\&\cdot\iint_{\mathcal{D}_O}\left[\varepsilon_r(\boldsymbol{\rho}')-\overline{\varepsilon}_r(\boldsymbol{\rho}')\right]\overline{G}(\boldsymbol{\rho}',\boldsymbol{\rho})G(\boldsymbol{\rho}',\boldsymbol{\rho}_S)dA(\boldsymbol{\rho}').\end{aligned} \tag{9}$$

Equation (9) is one possible form of a *field equation* and is still exact. Substituting this expression in (8) results in

$$\begin{aligned}&G(\boldsymbol{\rho}_R,\boldsymbol{\rho}_S)-\overline{G}(\boldsymbol{\rho}_R,\boldsymbol{\rho}_S)\\&\quad=-\frac{s^2}{c_0^2}\iint_{\mathcal{D}_O}\left[\varepsilon_r(\boldsymbol{\rho})-\overline{\varepsilon}_r(\boldsymbol{\rho})\right]\overline{G}(\boldsymbol{\rho},\boldsymbol{\rho}_R)\overline{G}(\boldsymbol{\rho},\boldsymbol{\rho}_S)\,dA(\boldsymbol{\rho})\\&\qquad+\Delta G(\boldsymbol{\rho}_R,\boldsymbol{\rho}_S).\end{aligned} \tag{10}$$

The first term on the right-hand side is the so-called *distorted-wave Born approximation* of the left-hand side. The

second term is the error in the approximation, also referred to as the *Born error*. This error can be written as

$$\Delta G(\boldsymbol{\rho}_R, \boldsymbol{\rho}_S) = \frac{s^4}{c_0^4} \iint_{\mathcal{D}_O} [\varepsilon_r(\boldsymbol{\rho}) - \overline{\varepsilon}_r(\boldsymbol{\rho})]\, \overline{G}(\boldsymbol{\rho}, \boldsymbol{\rho}_R) \cdot \left\{ \iint_{\mathcal{D}_O} [\varepsilon_r(\boldsymbol{\rho}') - \overline{\varepsilon}_r(\boldsymbol{\rho}')] \cdot \overline{G}(\boldsymbol{\rho}', \boldsymbol{\rho})\, G(\boldsymbol{\rho}', \boldsymbol{\rho}_S)\, dA(\boldsymbol{\rho}') \right\} dA(\boldsymbol{\rho}). \tag{11}$$

From the expression in (11), it is immediately observed that $\Delta G(\boldsymbol{\rho}_R, \boldsymbol{\rho}_S) = \mathcal{O}([\varepsilon_r - \overline{\varepsilon}_r]^2)$ as $|\varepsilon_r - \overline{\varepsilon}_r| \to 0$. Therefore, neglecting the term $\Delta G(\boldsymbol{\rho}_R, \boldsymbol{\rho}_S)$ in (10) is indeed a linearization of the data equation. The quality of this linearization will be discussed in Section IV-A.

B. Iterative Procedure

With the theory given above, we are now in a position to formulate our version of the distorted-wave-Born iterative procedure. In each iteration step, we start from a previously estimated, parameterized permittivity profile $\tilde{\varepsilon}_r^{(n-1)}(\boldsymbol{\rho})$ of the form (6). For sources at $\boldsymbol{\rho}_P \in \partial\mathcal{D}_O$, we determine the fields $\tilde{G}^{(n-1)}(\boldsymbol{\rho}, \boldsymbol{\rho}_P)$ that would be present in $\mathcal{D}_O$ in this configuration.

To this end, we return to the integral relation (5). In this relation, we choose $\varepsilon_r(\boldsymbol{\rho}) = \tilde{\varepsilon}_r^{(n-1)}(\boldsymbol{\rho})$, $\overline{\varepsilon}_r(\boldsymbol{\rho}) = \varepsilon_{1r}$ and $\boldsymbol{\rho} \in \mathcal{D}_O$. This results in the integral equation

$$\tilde{G}^{(n-1)}(\boldsymbol{\rho}, \boldsymbol{\rho}_P) = G_1(\boldsymbol{\rho}, \boldsymbol{\rho}_P) - \frac{s^2}{c_0^2} \iint_{\mathcal{D}_O} \tilde{\chi}^{(n-1)}(\boldsymbol{\rho}')\, G_1(\boldsymbol{\rho}, \boldsymbol{\rho}') \cdot \tilde{G}^{(n-1)}(\boldsymbol{\rho}', \boldsymbol{\rho}_P)\, dA(\boldsymbol{\rho}'). \tag{12}$$

In (12), $\tilde{\chi}^{(n-1)}(\boldsymbol{\rho})$ is the susceptibility as introduced in (6), and G_1 is Green's function of the surrounding medium

$$G_1(\boldsymbol{\rho}, \boldsymbol{\rho}') = \frac{1}{2\pi} K_0\left(\frac{s}{c_1} |(\boldsymbol{\rho} - \boldsymbol{\rho}'|\right) \tag{13}$$

where K_0 denotes the modified Bessel function of the second kind of order zero. The advantage of choosing this integral equation is that both the incident field and the Green's function in (12) are available in closed form.

Next, we use the integral relation (12) for $\boldsymbol{\rho} = \boldsymbol{\rho}_R$ and $\boldsymbol{\rho}_P = \boldsymbol{\rho}_S$ to obtain the field on $\partial\mathcal{D}_O$. For this field, we use the distorted-wave Born approximation (10) to derive the linearized equation

$$G(\boldsymbol{\rho}_R, \boldsymbol{\rho}_S) - \tilde{G}^{(n-1)}(\boldsymbol{\rho}_R, \boldsymbol{\rho}_S) = -\frac{s^2}{c_1^2} \iint_{\mathcal{D}_O} \sum_\alpha \left[\tilde{\chi}_\alpha^{(n)} - \tilde{\chi}_\alpha^{(n-1)}\right] \psi_\alpha(\boldsymbol{\rho}) \cdot \tilde{G}^{(n-1)}(\boldsymbol{\rho}, \boldsymbol{\rho}_R)\, \tilde{G}^{(n-1)}(\boldsymbol{\rho}, \boldsymbol{\rho}_S)\, dA(\boldsymbol{\rho}). \tag{14}$$

In this equation the "profile update," represented by the coefficients $\{\tilde{\chi}_\alpha^{(n)} - \tilde{\chi}_\alpha^{(n-1)}\}$, is determined by minimizing a cost function of the form (7). This results in a subsequent estimate of the unknown profile $\varepsilon_r^{(n)}(\boldsymbol{\rho})$, which allows us to carry out the next iteration step. Formulated in this manner, the distorted-wave-Born iterative procedure is also identical to the so-called Newton–Kantorovitch method. For the discrete form of the algorithm, this was first shown in [9]. An analysis in operator form can be found in [10].

IV. Linearized Scheme: Fundamental Aspects

The formulation of the iterative procedure in Section III-B leaves us with two fundamental questions. Will the scheme converge and what resolution can we expect upon convergence? For the dielectric slab, these questions were addressed in [1], [2] with the aid of WKB theory. For the present configuration, we have only partial answers. Nevertheless, these answers are needed to justify the numerical implementation discussed in Section V. In the present section, we discuss both these questions.

A. Dynamic Range

The question of convergence depends critically on the quality of the distorted-wave Born approximation in the first iteration step. To be more specific, the "profile update" in each iteration step is determined by matching the linear term in $[\varepsilon_r(\boldsymbol{\rho}) - \overline{\varepsilon}_r(\boldsymbol{\rho})]$ in (10) to the difference $G(\boldsymbol{\rho}_R, \boldsymbol{\rho}_S) - \overline{G}(\boldsymbol{\rho}_R, \boldsymbol{\rho}_S)$. Therefore, the issue is how well that difference is actually approximated. To quantify this in a single number, we introduce the root mean square error (RMSE)

$$\text{ERR} = \sqrt{\frac{\int_{-\pi}^{\pi} d\phi_R \int_{-\pi}^{\pi} d\phi_S\, |G(\boldsymbol{\rho}_R, \boldsymbol{\rho}_S) - G^B(\boldsymbol{\rho}_R, \boldsymbol{\rho}_S)|^2}{\int_{-\pi}^{\pi} d\phi_R \int_{-\pi}^{\pi} d\phi_S\, |G(\boldsymbol{\rho}_R, \boldsymbol{\rho}_S) - \overline{G}(\boldsymbol{\rho}_R, \boldsymbol{\rho}_S)|^2}} \times 100\% \tag{15}$$

where $G^B(\boldsymbol{\rho}_R, \boldsymbol{\rho}_S)$ is the distorted-wave-Born approximation that is obtained by neglecting $\Delta G(\boldsymbol{\rho}_R, \boldsymbol{\rho}_S)$ in (10). This choice of error has the advantage that it indicates the relative accuracy even when $s = j\omega$ and/or $\varepsilon_r(\boldsymbol{\rho}) - \overline{\varepsilon}_r(\boldsymbol{\rho})$ are small.

As mentioned above, a general estimate of the behavior of the error defined in (15) is hard to give. Therefore, we restrict ourselves to a parameter study for a canonical problem where this error can be evaluated in closed form. In Figs. 2–5, we present results for the case where the actual and the estimated configurations are concentric, homogeneous, lossless circular cylinders with relative permittivity ε_{2r} and $\overline{\varepsilon}_{2r}$ and radius a and $\overline{a}$, respectively. In both configurations, the surrounding medium is free space. The relevant theory is summarized in Appendix B. Here, we concentrate on the results.

In Figs. 2–5, we consider the influence of three properties of our setup.

- *Operating frequency.* In Fig. 2, we consider the Born error as a function of the normalized frequency $\omega a/c_0$ (with

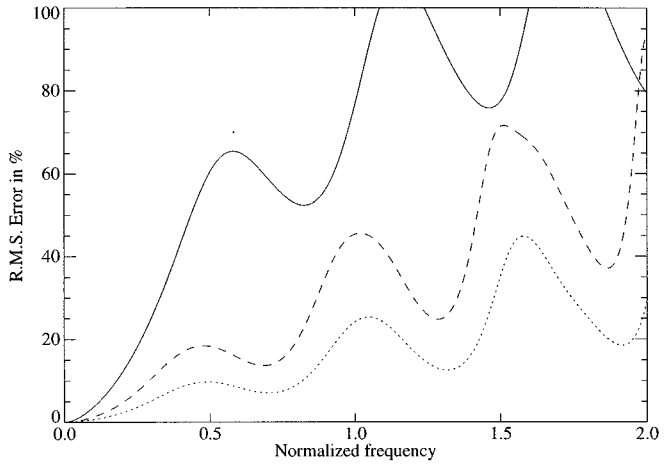

Fig. 2. Born error as a function of the normalized frequency $\omega a/c_0$ for a circular configuration with $a = \overline{a} = 1$ m, $\rho_O = 1.5$ m and $\varepsilon_{2r} = 5$. Solid line $\overline{\varepsilon}_{2r} = 2$; dotted line $\overline{\varepsilon}_{2r} = 5.5$; dashed line $\overline{\varepsilon}_{2r} = 6$.

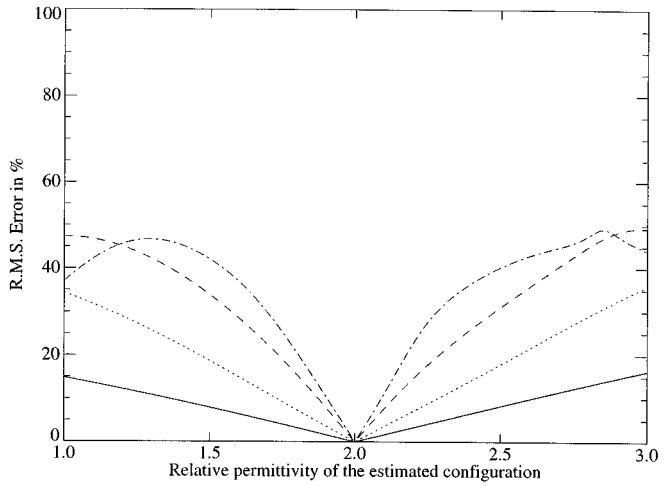

Fig. 3. Born error as a function of the estimated permittivity $\overline{\varepsilon}_2$ for a circular configuration with $a = \overline{a} = 1$ m, $\rho_O = 3$ m and $\varepsilon_{2r} = 2$. Solid line $f = 30$ MHz; dotted line $f = 100$ MHz; dashed line $f = 200$ MHz; dash-dot line $f = 300$ MHz.

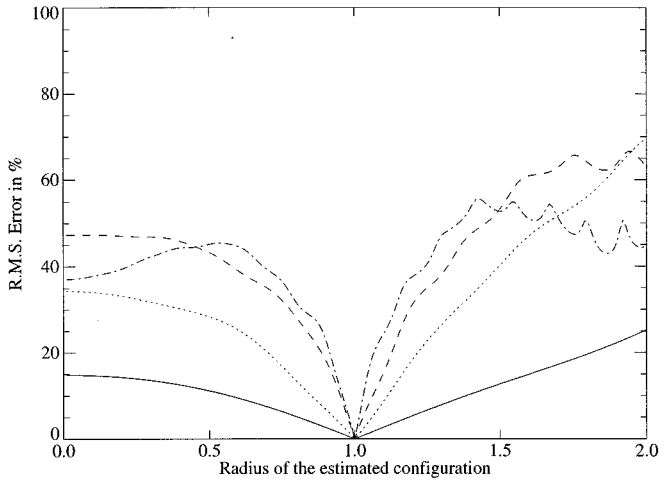

Fig. 4. Born error as a function of the estimated radius $\overline{a}/a$ for a circular configuration with $a = 1$ m, $\rho_O = 3$ m and $\varepsilon_{2r} = \overline{\varepsilon}_{2r} = 2$. Solid line $f = 30$ MHz; dotted line $f = 100$ MHz; dashed line $f = 200$ MHz; dash-dot line $f = 300$ MHz.

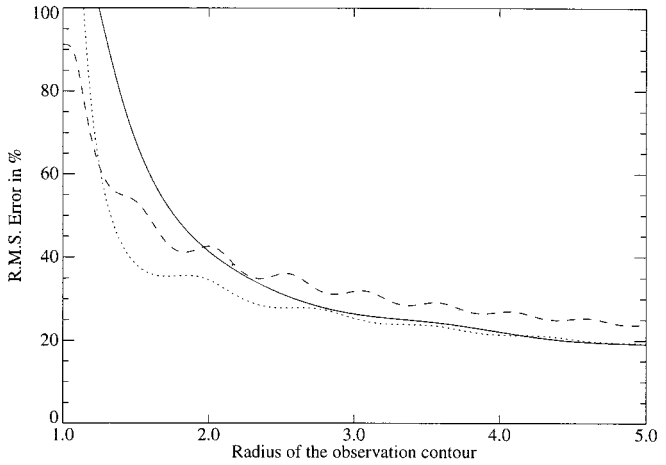

Fig. 5. Born error for an observation contour with varying ρ_O/a for a circular configuration with $a = \overline{a} = 1$ m, $\varepsilon_{2r} = 6$ and $\overline{\varepsilon}_{2r} = 5.5$. Solid line $f = 100$ MHz; dotted line $f = 200$ MHz; dashed line $f = 300$ MHz.

$s = j\omega$) for two cylinders with $a = \overline{a} = 1$ m and $\rho_O = 1.5$ m. The exact configuration has a relative permittivity of $\varepsilon_{2r} = 5.0$, and the estimated permittivities are $\overline{\varepsilon}_{2r} = 2.0$, 5.5, and 6.0, respectively. All three curves show a linear increase until the approximation becomes meaningless. Further, the slope increases with increasing $|\overline{\varepsilon}_{2r} - \varepsilon_{2r}|$. The oscillations may be associated with resonances of the exact and the estimated configuration.

- *Contrast.* In Fig. 3, we consider the influence of the relative permittivity of the estimated configuration. The cylinders have $a = \overline{a} = 1$ m, the actual permittivity is $\varepsilon_{2r} = 2$, the observation is at $\rho_O = 3$ m, and the lines are for $\omega = 2\pi f$ with $f = 30$, 100, 200, and 300 MHz. Similarly, Fig. 4 shows results of varying $\overline{a}$ for $\overline{\varepsilon}_{2r} = 2.0$ and other parameters as in Fig. 4. From these figures, we conclude that the Born error increases linearly with increasing contrast, with a slope determined by the operating frequency.
- *Observation.* In Fig. 5, we consider the influence of the choice of ρ_O for $a = \overline{a} = 1$ m, $\varepsilon_{2r} = 6$, $\overline{\varepsilon}_{2r} = 5.5$, and $f = 100$, 200, and 300 MHz. Fig. 5 indicates that we should not choose the observation contour too close to the scattering obstacle. A possible explanation is that, in that region, the evanescent field plays an important role. For observation further away from the cylinder, the quality of the Born approximation is almost independent of the value of ρ_O.

Summarizing, the dynamic range of the Born-type iterative procedure appears to be determined by $\omega\,||\varepsilon_r - \varepsilon_r^{(0)}||$, where $||\cdot||$ is the L_1 norm.

B. Resolution

The second question is how much information can be retrieved from the linearized equation. To keep the discussion tractable, we again restrict ourselves to lossless media. We assume that the reference profile $\overline{\varepsilon}_r(\boldsymbol{\rho})$ is a smooth estimate of the actual profile $\varepsilon_r(\boldsymbol{\rho})$, and that the difference between both profiles is so small that the distorted-wave-Born approximation is almost exact. Further, we take $s = j\omega$.

In that case, we can invoke the following argument, which has been inspired by [27] and by the back-propagation algorithm as applied in geophysical imaging. The data equation (10) is now linear in $\varepsilon_r(\boldsymbol{\rho})-\overline{\varepsilon}_r(\boldsymbol{\rho})$. Therefore, we may consider the situation where

$$\varepsilon_r(\boldsymbol{\rho}) = \overline{\varepsilon}_r(\boldsymbol{\rho}) + p(\boldsymbol{\rho}) \tag{16}$$

where $p(\boldsymbol{\rho})$ is a "pixel" centered around a point $\boldsymbol{\rho} = \boldsymbol{\rho}_O$ in $\mathcal{D}_O$. We assume that $p(\boldsymbol{\rho})$ has a finite support Δ_O that is small enough to treat $\overline{\varepsilon}_r(\boldsymbol{\rho})$ as a constant, i.e., $\overline{\varepsilon}_r(\boldsymbol{\rho}) = \overline{\varepsilon}_r(\boldsymbol{\rho}_O)$ when $\boldsymbol{\rho} \in \Delta_O$. In that case, the unit-amplitude plane wave

$$\overline{E}(\boldsymbol{\rho}, \phi^i) = \exp\left(-\frac{j\omega}{c_0}\sqrt{\overline{\varepsilon}_r(\rho_O)}\,(\boldsymbol{\rho}\cdot\mathbf{u}^i)\right) \tag{17}$$

is a valid solution of the second-order differential equation (2) for the reference medium in Δ_O. The angle ϕ^i may be viewed upon as an angle of incidence in the equivalent problem with the pixel in a homogeneous environment.

Now the solution $\overline{E}(\boldsymbol{\rho}, \phi^i)$ has a unique continuation in any source-free region enclosing Δ_O, and in particular in $\mathcal{D}_O$ [28]. It may not be easy to compute this continuation for a general configuration, but it does exist. As argued in Appendix A, this means that for $a\sqrt{2} < \rho < \rho_O$ this solution can be written in the form of a Fourier representation

$$\overline{E}(\boldsymbol{\rho}, \phi^i) = \sum_{m=-\infty}^{\infty}\left[A_m I_m\left(\frac{s}{c_1}\rho\right) + B_m K_m\left(\frac{s}{c_1}\rho\right)\right]\exp(jm\phi). \tag{18}$$

Using the equivalence principle formulated in (A.5), we can then express $\overline{E}(\boldsymbol{\rho}, \phi^i)$ as a linear combination of Green's functions

$$\overline{E}(\boldsymbol{\rho}, \phi^i) = \int_{-\pi}^{\pi} w(\phi_S, \phi^i)\,\overline{G}(\boldsymbol{\rho}, \boldsymbol{\rho}_S)\,d\phi_S. \tag{19}$$

In (19), ϕ^i may assume any value in the interval $-\pi < \phi^i \leq \pi$. Introducing an observation angle ϕ^o, we can therefore invoke (10) to obtain

$$\int_{-\pi}^{\pi} d\phi_R \int_{-\pi}^{\pi} d\phi_S w(\phi_R, -\phi^o)\, w(\phi_S, \phi^i) \cdot \left[G(\boldsymbol{\rho}_R, \boldsymbol{\rho}_S) - \overline{G}(\boldsymbol{\rho}_R, \boldsymbol{\rho}_S)\right] = \frac{\omega^2}{c_0^2}\iint_{\Delta_O} p(\boldsymbol{\rho}) \cdot \exp\left(\frac{j\omega}{c_0}\sqrt{\overline{\varepsilon}_r(\rho_O)}\,(\boldsymbol{\rho}\cdot[\mathbf{u}^o - \mathbf{u}^i])\right) dA(\boldsymbol{\rho}) \tag{20}$$

where the right-hand side may be recognized as a spatial Fourier transform (FT) of $p(\boldsymbol{\rho})$. Following the same lines as in the classical Ewald theory for a homogeneous background medium then leads to the conclusion that this spatial FT can be determined up to $k_{\max} = 2\omega\sqrt{\overline{\varepsilon}_r(\rho_O)}/c_0$. Since the field $G(\boldsymbol{\rho}_R, \boldsymbol{\rho}_S)$ contains this information, a minimization of the cost function (7) will attempt to generate a reconstructed profile with the correct FT up to this limit. This leads to the usual concept of a *point-spread function*, but this function now depends on the local value $\overline{\varepsilon}_r(\boldsymbol{\rho}_O)$.

As an illustration, we consider in Fig. 6 the reconstruction of a circularly symmetric configuration with a small contrast with respect to a homogeneous cylinder with radius $a = 1$ m in free space. We consider the reconstruction of a radially inhomogeneous permittivity

$$\varepsilon_{2r}(\rho) = \overline{\varepsilon}_{2r} + \begin{cases} 0.003 & 0 \leq \rho < a/4, \\ 0.002 & a/4 < \rho < a/2, \\ 0.001 & a/2 < \rho < 3a/4, \\ 0 & 3a/4 < \rho < a \end{cases} \tag{21}$$

from the scattered field at 64 equally spaced source and receiver positions at $\rho_O = 1.1$ m. The direct problem was solved by numerically integrating two coupled first-order differential equations for the coefficients in a Fourier representation of the form (B.3) [29]. The images were generated by using (B.14) and (B.15) to identify the Fourier coefficients of the weighting function $w(\phi, \phi^i)$, interpolating in cylindrical coordinates in wavenumber space to obtain sampled values of (20) on a Cartesian grid, and applying a 2-D FFT to obtain the permittivity contrast.

Fig. 6(a) shows the reconstruction for $\overline{\varepsilon}_{2r} = 1$, i.e., a susceptibility profile in free space for $f = 200$ MHz. In Fig. 6(b) and (d), we improve the resolution by raising the frequency to 500 MHz and 1 GHz, respectively. In Fig. 6(c) and (e), we keep the frequency fixed and raise the permittivity of the reference medium inside the cylinder to $\overline{\varepsilon}_{2r} = 6.25$ and $\overline{\varepsilon}_{2r} = 25$, respectively. The results confirm that the parameter $\omega\sqrt{\overline{\varepsilon}_{2r}}/c_0$ determines the reconstruction. Finally, it should be remarked that reconstructions of this quality could only be obtained for this special configuration because an exact theory was available.

C. Multiple Frequencies

The results presented in the previous two subsections lead to the following conclusions. Ideally, any reconstruction procedure should be started from a homogeneous space, i.e., from $\varepsilon_r^{(0)}(\boldsymbol{\rho}) = \varepsilon_{1r}$. Thus, the only *a priori* knowledge is the fact that the scatterer is located in $\mathcal{D}_O$. However, especially for large contrasts, this imposes a restriction on the maximum value of ω. This restriction, in turn, limits the resolution with which $\varepsilon_{2r}(\boldsymbol{\rho})$ is reconstructed upon convergence.

Therefore, we use multiple frequencies. The first approximation of the unknown permittivity profile is indeed obtained starting from $\varepsilon_r^{(0)}(\boldsymbol{\rho}) = \varepsilon_{1r}$. When the restrictions on ω imposed by this choice are too severe, we use this approximation as a starting value for a reconstruction at a larger value of ω. By gradually increasing the operating frequency, we are then able to determine the required detail of the configuration, even for large contrasts in permittivity between the cylinder and the surrounding free space. Of course, increasing the frequency requires

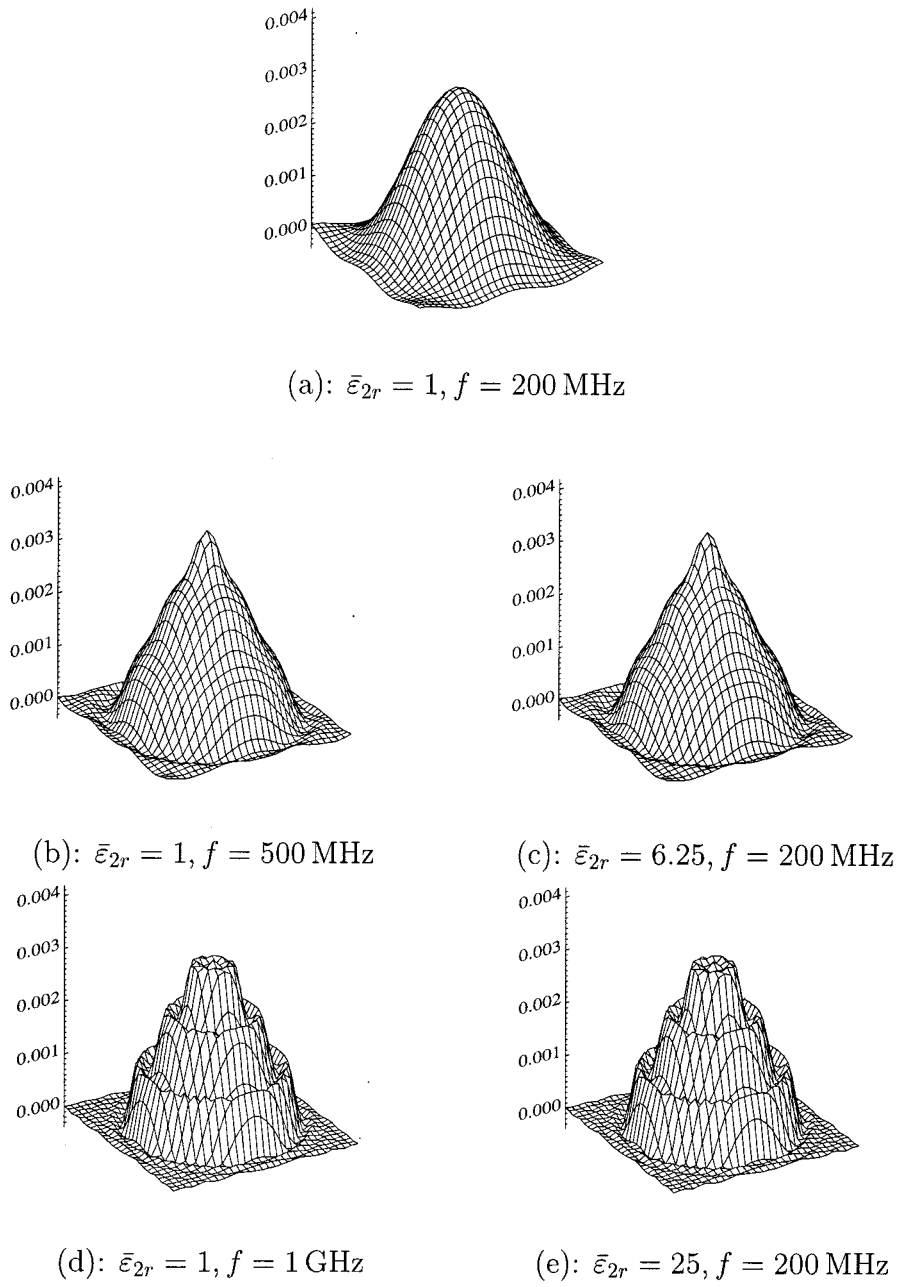

Fig. 6. Reconstruction of a small permittivity contrast as specified in (21) for $a = 1$ m, $\rho_O = 1.1$ m and other parameters as indicated.

scaling the imaginary part of $\varepsilon_r(\boldsymbol{\rho})$. In practice, the assumption of a Maxwellian model generally leads to acceptable results.

The use of multiple-frequency information as proposed above implicitly relies on the assumption that the spatial FT $\hat{\chi}(\mathbf{k})$ of $\chi(\boldsymbol{\rho})$ decreases in magnitude with increasing k. This assumption holds for most practical profiles, but may be violated in pathological cases. Finally, the multiple-frequency procedure also supplies the answer to the one remaining question from the resolution analysis of Section IV-B, i.e., the choice of the smooth estimate $\overline{\varepsilon}(\boldsymbol{\rho})$. At each new frequency, the final result for the previous frequency may be considered as that estimate. This result is then used to choose the smallest spacing with which we expect to reconstruct the unknown permittivity somewhere in $\mathcal{D}_O$. Applying the reconstruction algorithm will then gradually produce more detailed knowledge of the unknown profile.

V. Linearized Schemes: Numerical Implementation

Now that we have gained some insight into the capabilities of the distorted-wave iterative Born procedure, we need to address its numerical implementation. We follow the same order as in the actual computation. In Section V-A, we discuss the determination of the fields in the actual and estimated configurations. In Section V-B, we discuss the translation of the theoretical results into the numerical determination of the profile update. In Section V-C, our approach is validated for a representative configuration.

A. Forward Problem

The feasibility of iterative schemes for the solution of inverse-scattering problems based on optimizing a parameterized

configuration depends strongly on the availability of a fast procedure for determining the fields in the estimated geometry in successive iteration steps. For the present configuration, such a scheme is available from [25]. Starting point is the contrast-source integral equation

$$G(\boldsymbol{\rho}, \boldsymbol{\rho}_P) = G_1(\boldsymbol{\rho}, \boldsymbol{\rho}_P) - \frac{s^2}{c_0^2} \iint_{\mathcal{D}_2} \chi(\boldsymbol{\rho}')\, G_1(\boldsymbol{\rho}, \boldsymbol{\rho}') G(\boldsymbol{\rho}', \boldsymbol{\rho}_P)\, dA(\boldsymbol{\rho}') \tag{22}$$

where $G_1(\boldsymbol{\rho}, \boldsymbol{\rho}')$ is given by (13) and $\chi(\boldsymbol{\rho}) = \varepsilon_r(\boldsymbol{\rho}) - \varepsilon_{1r}$. The region $-a < x < a$, $-a < y < a$, in which $\mathcal{D}_2$ is embedded, is subdivided into $N \times N$ square subregions with mesh size $h = 2a/N$. The grid points of the square mesh are located at $\boldsymbol{\rho}_{n,m} = x_n\, \mathbf{u}_x + y_m \mathbf{u}_y$, with $x_n = -a + nh$ for $n = 0, 1, \ldots, N$, and $y_m = -a + mh$ for $m = 0, 1, \ldots, N$. Solving (22) now amounts to determining an approximation of $G(\boldsymbol{\rho}, \boldsymbol{\rho}_P)$ at the grid points $\boldsymbol{\rho} = \boldsymbol{\rho}_{n,m}$.

The space discretization of the integral in the right-hand side of (22) has two special aspects. First, the logarithmically singular behavior of $K_0(sR/c_1)$ as $R = |\boldsymbol{\rho} - \boldsymbol{\rho}'| \downarrow 0$ is substracted by breaking up the integral over $\mathcal{D}_2$ into

$$\iint_{\mathcal{D}_2} \left\{ K_0\left(\frac{sR}{c_1}\right) + \ln\left(\frac{R}{a}\right) \right\} \chi(\boldsymbol{\rho}')\, G(\boldsymbol{\rho}', \boldsymbol{\rho}_P)\, dA(\boldsymbol{\rho}') - \iint_{\mathcal{D}_2} \ln\left(\frac{R}{a}\right) \chi(\boldsymbol{\rho}')\, G(\boldsymbol{\rho}', \boldsymbol{\rho}_P)\, dA(\boldsymbol{\rho}'). \tag{23}$$

Second, the discretization of the integrals in (23) is based on approximating suitable parts of the integrands by piecewise-linear interpolation, and integrating analytically over polygons determined by the boundary of $\mathcal{D}_2$ and the grid. This results in a discretized integral equation of the form

$$G[n, m] = G_1(\boldsymbol{\rho}_{n,m}, \boldsymbol{\rho}_S) - \frac{s^2 h^2}{2\pi c_0^2} \sum_{n'=0}^{N} \sum_{m'=0}^{N} K\left[|n - n'|, |m - m'|\right] \cdot \chi[n', m']\, G[n', m'] \tag{24}$$

where $\chi[n', m']$ is a sampled, filtered version of $\chi(\boldsymbol{\rho})$. In (24), the convolution-type structure of the continuous (22) has been preserved. This makes this equation suitable for the application of the conjugate-gradient-FFT method. In addition, it is second-order accurate in the mesh size h.

The initial estimate for this procedure is obtained by taking a linear combination of previous "final" solutions and determining the coefficients by minimizing the squared error for the problem at hand. This idea was first suggested as "marching on in frequency" for the computation of transient fields in [24] and [25]. In [26], a more detailed explanation is given, as well as several examples of other physical parameters for which the effectiveness of this extrapolation has been demonstrated. In the iterative procedure formulated in Section III-B, we extrapolate in source position for the first two steps of the distorted-wave-Born iterative procedure. Subsequently, we use the fields for the exact source position in the previous two estimated configurations to generate the initial estimate for the field in the configuration at hand. This is referred to as "marching on in source position" and "marching on in profile," respectively.

As mentioned in Section II-A, the boundary information is only used in generating the scattered-field data for the exact profile. Further, scattered fields were used for a homogeneous (Appendix B) or radially inhomogeneous [29] circular cylinder, which is positioned eccentrically inside the observation contour. In both cases "inverse crimes" are avoided inherently.

B. Update Step

The second part of each step in the distorted-wave Born approximation is the determination of the "profile update." In our implementation, the parameterization of the contrast function $\tilde{\chi}(\boldsymbol{\rho})$ in (6) is chosen such that this function is approximated by a piecewise bilinear expansion in $-a < x < a$ and $-a < y < a$

$$\tilde{\varepsilon}_r(\boldsymbol{\rho}) = \varepsilon_{1r} + \sum_{k=0}^{K} \sum_{\ell=0}^{K} \tilde{\chi}_{k,\ell}\, \Lambda(x - x_{kM})\, \Lambda(y - y_{\ell M}) \tag{25}$$

with x_n and y_m being the same discrete coordinates as in the space discretization of the forward problem and $K = N/M$, Thus, the mesh size in the field computation is M times smaller than the one in the profile update. $\Lambda(\xi)$ is a triangular expansion function

$$\Lambda(\xi) = \begin{cases} 1 - |\xi|/Mh, & \text{for } |\xi| < Mh, \\ 0, & \text{otherwise.} \end{cases} \tag{26}$$

The approximation (25) is substituted in the Born-approximated equation (14), and the coefficients $\{\tilde{\chi}_{k,\ell}^{(n)} - \tilde{\chi}_{k,\ell}^{(n-1)}\}$ are determined by minimizing the squared error (7).

The final issue is the choice of the number of subintervals K in the representation of the contrast function in (25). This choice follows from the resolution analysis of Section IV-B. This analysis has revealed that the resolution depends on the local average of the refractive index $\sqrt{\bar{\varepsilon}_r(\rho)}$. Therefore, if we want to obtain maximum resolution where this index is large, the representation (25) will be oversampled where this index is smaller. This ambiguity is removed by augmenting the cost function in (7) with the *regularization* term

$$\delta \left(\frac{K}{2a\rho_O}\right)^2 \left\{ \sum_{k=1}^{K-1} \sum_{\ell=0}^{K} (\tilde{\chi}_{k-1,\ell} - 2\tilde{\chi}_{k,\ell} + \tilde{\chi}_{k+1,\ell})^2 + \sum_{k=0}^{K} \sum_{\ell=1}^{K-1} (\tilde{\chi}_{k,\ell-1} - 2\tilde{\chi}_{k,\ell} + \tilde{\chi}_{k,\ell+1})^2 \right\}. \tag{27}$$

In (27), δ is a small parameter. The terms in (27) restrict the variation in derivative in the x- and y-directions between adjacent cells. The factor of $(K/2a\,\rho_O)^2$ ensures that the relative importance of the regularization term becomes independent of K and ρ_O. The factor of ρ_O^{-2} can be envisaged as changing the integrals in (7) into path integrals over the observation contour and compensates for the decrease of $G(\boldsymbol{\rho}_R, \boldsymbol{\rho}_S)$ with increasing ρ_O. The factor of $(K/2a)^2$ makes (27) approximately proportional to a

double integral over $\mathcal{D}_O$ of the squares of $\partial_x^2\chi(\boldsymbol{\rho})$ and $\partial_y^2\chi(\boldsymbol{\rho})$. Thus, the smoothing effect of (27) remains invariant in a multigrid reconstruction. The regularization term (27) pertains to the total susceptibility and not to the profile update. Particularly, in the presence of noise, this choice avoids a possible dependence of the final result on the initial estimate.

Including (27) with a large value of δ is an alternative to using multiple-frequency information for obtaining the "trend" of $\chi(\boldsymbol{\rho})$, which can then be used as an initial estimate for reconstructing the available "detail." Finally, it should be mentioned that the minimum of the combined cost function is again searched with the aid of the conjugate-gradient method.

C. Examples

A large number of numerical experiments were carried out to validate the theory and the algorithms presented in the previous sections. As an illustration, we present in Fig. 7 results for the Österreich profile, which was first discussed at a PIERS meeting in Austria [20] and has since been studied by a number of groups in Europe (see e.g., [21]). The configuration consists of a large circular cylinder of radius 0.6 m with a hole of radius 0.3 m, flanked by two small circular cylinders of radius 0.2 m. The surrounding medium was free space and the relative permittivity inside the object was $\varepsilon_{2r} = 2$, i.e., $\chi = 1$. As mentioned in the introduction, we consider a lossless configuration to avoid the discussion of dispersion effects. The scattered field was computed with $N = 64$ for 64 source and receiver positions on an observation contour with radius $\rho_O = 3$ m. Fig. 7a shows the discretized susceptibility for the forward field computations. Fig. 7(b) shows the reconstruction for $f = 300$ MHz with $\delta = 10^{-8}$ for the first five iterations, and $\delta = 10^{-9}$ for subsequent steps, starting from $\chi(\boldsymbol{\rho}) = 0$. Fig. 7(c) shows the reconstruction for $f = 500$ MHz with $\delta = 10^{-9}$, starting from the reconstruction for $f = 300$ MHz. An attempt to reconstruct this profile directly for $f = 500$ MHz, starting from $\chi(\boldsymbol{\rho}) = 0$, was unsuccessful.

Similar results were also obtained for larger contrasts. Reconstructing such configurations does require smaller frequency steps. Space limitations prevent us from including the results. Instead, we show in Fig. 8 results for reconstructing the same configuration as in Fig. 7 from data on a line. To include the effect that the smaller cylinders may be shaded by the larger one, the configuration has been turned upside down. The field computations were carried out for $N = 64$, and we had 64 receivers on a line of width 32 m at $y = 3$ m for an object in a square with $a = 1$ m. In both cases, the regularization parameter was $\delta = 10^{-5}$ in the first five iteration steps, and $\delta = 10^{-6}$ in the remaining ones. Although in particular the lateral resolution is poorer than for the case of complete data, the features of the scattering object can still be recognized very well. The results in Fig. 8 give an indication of how well an object in a half space can be reconstructed from measurements above that half space.

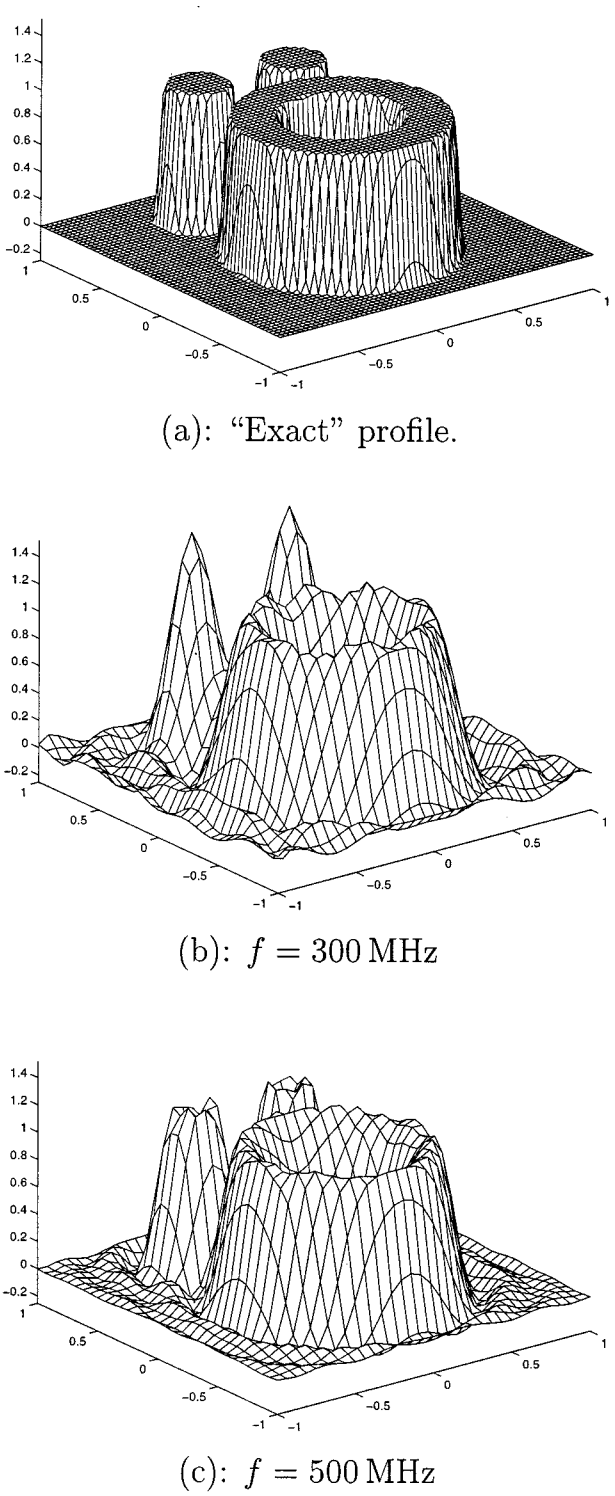

Fig. 7. Reconstructions of the Österreich profile as specified in the text. (a) Discretized susceptibility for forward problem with $N = 64$; (b) result after eight iterations for $f = 300$ MHz and $K = 32$ of the distorted-wave Born scheme starting from $\chi(\boldsymbol{\rho}) = 0$, and (c) result after two iterations for 500 MHz, starting from the estimate shown in (b).

VI. Nonlinear Optimization

The forward field computation as outlined in Section V-A is so efficient that, on average, updating the profile as described in Section V-B in each iteration step takes at least as much computation time as computing the fields. The dynamic range of such methods depends on the occurrence of local minima, which in turn seems to be determined by the size of the region in parameter space for which the cost function behaves as a quadratic function. This is exactly the region where the linearization introduced in Section III-A is a good approximation. Further, upon convergence, any nonlinear optimization scheme reduces to a

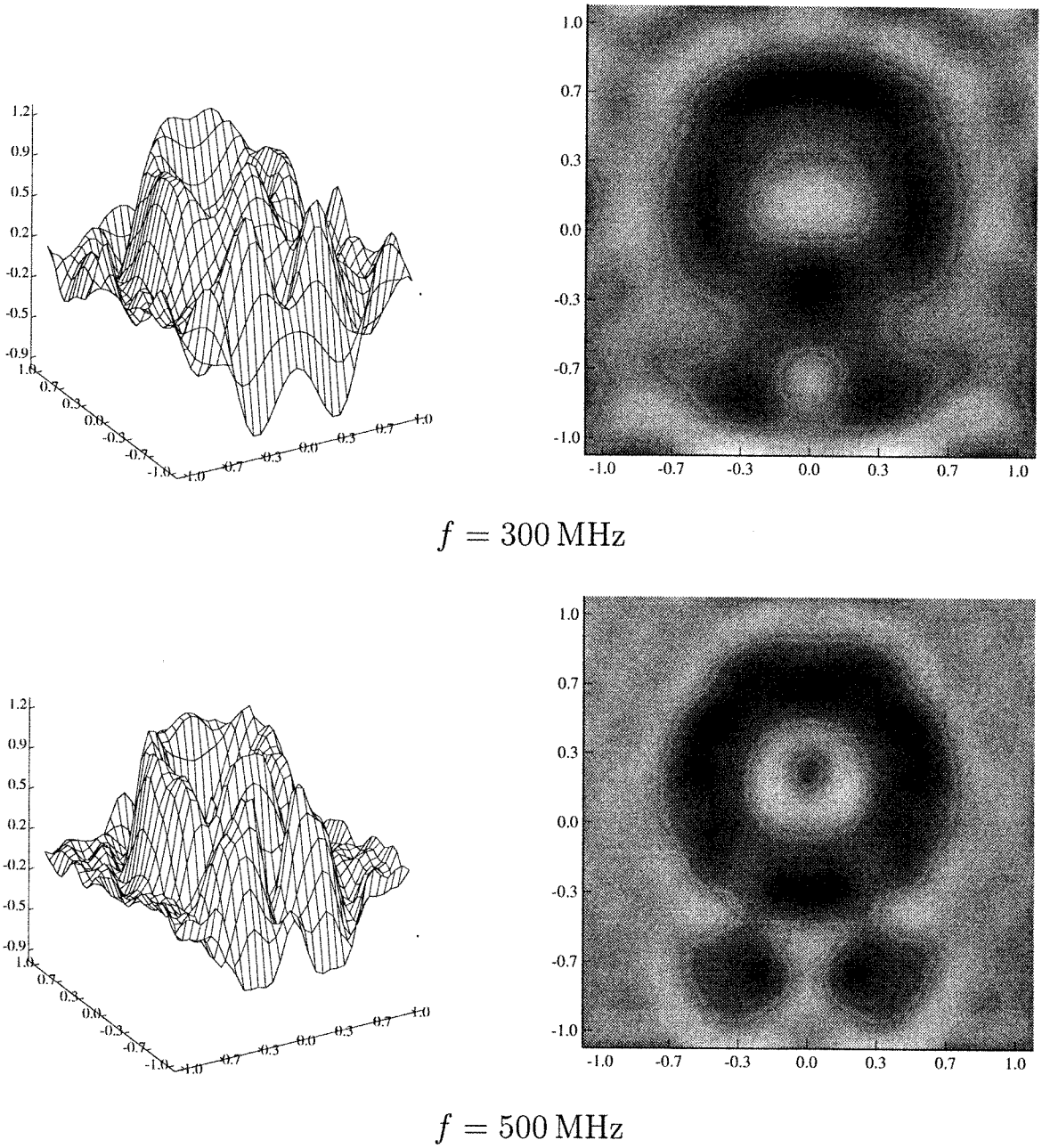

Fig. 8. Reconstructions of the inverted Österreich profile from data on a line. (Top) Result after 20 iterations for $f = 300$ MHz starting from $\chi(\boldsymbol{\rho}) = 0$. (Bottom) Result after 13 iterations for 500 MHz, starting from the result at $f = 300$ MHz.

linearized scheme, since higher-order terms in the Taylor series expansion of the cost function become negligible. Therefore, the stability and resolution of nonlinear schemes can still be assessed from the validity and the resolution of the linearized equation. This gives us all the elements for replacing the update step by a line search in a nonlinear optimization procedure. In the present context, we can only give a general description. Details will be published elsewhere.

A. Gradient of Cost Function

The first issue to be resolved in almost any nonlinear optimization scheme is the evaluation of the steepest-descent direction for a given estimate of the configuration $\overline{\varepsilon}_r(\boldsymbol{\rho})$ of the parameterized form specified in (6). Since $\tilde{\varepsilon}_r(\boldsymbol{\rho})$ is also of the form given in (6), we may rewrite the distorted-wave Born approximation of $\tilde{G}$ about $\overline{\varepsilon}_r$ as

$$\tilde{G}(\boldsymbol{\rho}_R, \boldsymbol{\rho}_S) = \overline{G}(\boldsymbol{\rho}_R, \boldsymbol{\rho}_S) - \frac{s^2}{c_0^2} \sum_{\alpha} (\tilde{\chi}_\alpha - \overline{\chi}_\alpha) \cdot \iint_{\mathcal{D}_O} \psi_\alpha(\boldsymbol{\rho}) \overline{G}(\boldsymbol{\rho}, \boldsymbol{\rho}_R) \overline{G}(\boldsymbol{\rho}, \boldsymbol{\rho}_S)\, dA(\boldsymbol{\rho}) + \mathcal{O}\left([\tilde{\chi} - \overline{\chi}]^2\right). \quad (28)$$

Substituting this result in (7) and interchanging the order of the integration then results in

$$J(\{\tilde{\chi}_\alpha\}) = J(\{\overline{\chi}_\alpha\}) + \sum_\alpha \mathrm{Re}\left[(\tilde{\chi}_\alpha - \overline{\chi}_\alpha)\iint_{\mathcal{D}_O} \psi_\alpha(\boldsymbol{\rho})\Gamma(\boldsymbol{\rho})\,dA(\boldsymbol{\rho})\right] + \mathcal{O}\left([\tilde{\chi} - \overline{\chi}]^2\right) \tag{29}$$

where the function $\Gamma(\boldsymbol{\rho})$ is the *profile gradient*

$$\Gamma(\boldsymbol{\rho}) = -\frac{2\,s^2}{c_0^2}\int_{-\pi}^{\pi} d\phi_R \int_{-\pi}^{\pi} d\phi_S \left\{\left[\overline{G}(\boldsymbol{\rho}_S, \boldsymbol{\rho}_R) - G(\boldsymbol{\rho}_S, \boldsymbol{\rho}_R)\right]^* \overline{G}(\boldsymbol{\rho}, \boldsymbol{\rho}_R)\overline{G}(\boldsymbol{\rho}, \boldsymbol{\rho}_S)\right\} \tag{30}$$

where $*$ means complex conjugation. Since our forward algorithm is capable of computing $\overline{G}(\boldsymbol{\rho}, \boldsymbol{\rho}_P)$ for $\boldsymbol{\rho}_P \in \partial\mathcal{D}_O$ at the cost of solving a few forward-scattering problems, the evaluation of $\Gamma(\boldsymbol{\rho})$ is very efficient.

Breaking up the parameters $\tilde{\chi}_\alpha$ into their real and imaginary parts according to $\tilde{\chi}_\alpha = \tilde{\chi}'_\alpha - j\tilde{\chi}_\alpha$ and using the limit definition of derivative then gives the following expressions for the gradient of $J(\tilde{\chi})$

$$\frac{\partial}{\partial \tilde{\chi}'_\alpha} J(\{\tilde{\chi}_\alpha\}) = \mathrm{Re}\iint_{\mathcal{D}_O} \psi_\alpha(\boldsymbol{\rho})\,\Gamma(\boldsymbol{\rho})\,dA(\boldsymbol{\rho}), \tag{31}$$

and

$$\frac{\partial}{\partial \tilde{\chi}''_\alpha} J(\{\tilde{\chi}_\alpha\}) = \mathrm{Im}\iint_{\mathcal{D}_O} \psi_\alpha(\boldsymbol{\rho})\,\Gamma(\boldsymbol{\rho})\,dA(\boldsymbol{\rho}). \tag{32}$$

Expressions similar to (31) and (32) can also be found in [8]. An independent verification of these expressions was obtained by differentiating $J(\{\tilde{\chi}_\alpha\})$, and using the field equation (22) and the reciprocity relation (4) to derive an expression for $(\partial/\partial\tilde{\chi}_\alpha)$ $G(\boldsymbol{\rho}, \boldsymbol{\rho}_S)$. For completeness, it should be mentioned that the gradient of the regularization term (27) is obtained directly in terms of the same real and imaginary parts.

B. Numerical Implementation

In our nonlinear optimization, we used the quasi-Newton method, with the Broyden–Fletcher–Goldfarb–Shanno or BFGS formulation of the Hessian [30]. The line-search algorithm consist of a bracketing phase, in which an acceptable search interval is supposed to be found, and a sectioning phase, in which this interval is divided into smaller brackets. In the forward scheme, we march in source position in the first two iterations of each line search. Subsequently, we use the feature that the parameter vector $\{\tilde{\chi}_\alpha\}$ is modified in a single direction to "march on in search direction." The resulting computation times are typically about twice as long as those of the linearized scheme.

Compared with linearized schemes, the quasi-Newton method has a slightly larger dynamic range. Multiple-frequency information or overregularization can still be used to improve convergence. When both schemes converge, the results are comparable. Nonlinear optimization is more stable with respect to noise and regularization only seems to be necessary in limiting cases. A possible explanation is that the quasi-Newton method repeatedly searches for the direction in $\{\tilde{\chi}_\alpha\}$-space, for which the cost function locally shows the strongest variation, while the distorted-wave-Born iterative procedure attempts to computes a fully detailed update of the vector $\{\tilde{\chi}_\alpha\}$ in each iteration step.

Fig. 9 shows an illustration of these effects. In this figure, we again attempt to reconstruct the Österreich profile, starting from the results at 300 MHz for the same algorithms, but with an operating frequency of $f = 700$ MHz. Compared with Fig. 7, the vertical scale was adjusted to display also the profile in Fig. 9(a), which shows the diverging result of five iteration steps with $\delta = 10^{-8}$ and five steps with $\delta = 10^{-9}$. In Fig. 9(b), the Born-type scheme was carried out for $\delta = 10^{-6}$, and $\delta = 10^{-7}$. In both cases, the results are unstable. Fig. 9(c) and (d) show results for eight iterations with the quasi-Newton scheme without regularization, and for two iterations with $\delta = 10^{-11}$.

VII. Conclusions

In this paper, we have analyzed linear and nonlinear iterative procedures for determining 2-D permittivity profiles in a homogeneous environment. Compared with related research, our work has two main points of attraction. First, the entire numerical implementation is based on a theoretical description, albeit an incomplete one. The theoretical analysis has led to ideas like using multiple-frequency data and making a consistent choice for the parameterization of the unknown profile and the regularization term in the cost function. Second, the combination of a second-order accurate space discretization that preserves the convolution structure of the continuous integral equation with the CGFFT algorithm and a special extrapolation procedure allows an extremely efficient computation of the fields in the successively estimated configurations. After the first few field computations, each new forward problem is solved in a few iterations of the classical CGFFT procedure. It is this efficiency that makes reconstruction schemes based on "exact" field computations feasible again, even compared with schemes of the modified-gradient type. In view of space limitations, we have not addressed the reconstruction of objects in more complex environments. However, an embedding scheme has already been implemented that translates the scattering operator for a homogeneous environment to a counterpart for a more practical environment.

Appendix A
Equivalence Theorems

In the text, we have twice used the feature that the total field in $\mathcal{D}_O$ and the scattered field in $\overline{\mathcal{D}}_O$ may be regarded as being generated by an equivalent surface source distribution on $\partial\mathcal{D}_O$. In this appendix, we discuss this property in more detail. We restrict ourselves to the case of complete data. For partial data, the analysis can be generalized by using a spatial FT with respect to the x-coordinate.

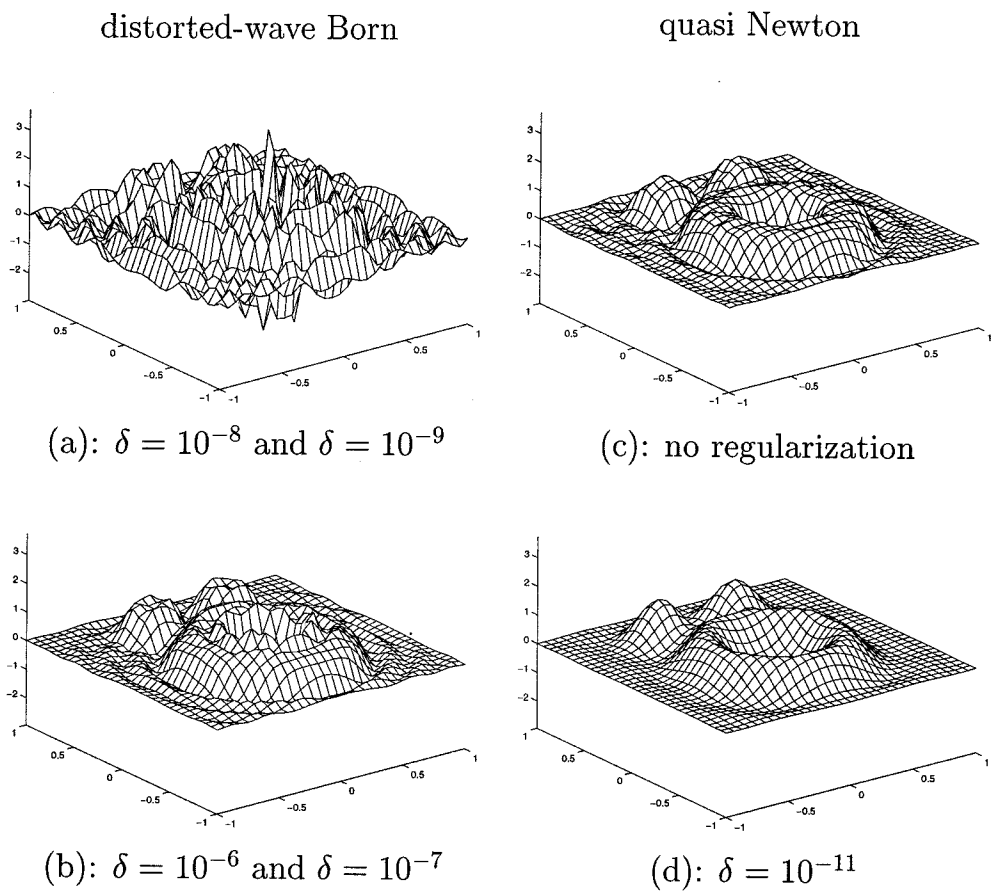

Fig. 9. Reconstructions at $f = 700$ MHz of the Österreich profile starting from the result displayed in Fig. 7(b).

From Fig. 1, it is clear that for $\rho \geq a\sqrt{2}$, the relative permittivity of the configuration is equal to ε_{1r}. In that region, we can write the counterpart of (2) for a surface current on $\partial\mathcal{D}_O$ as

$$\left[\partial_\rho^2 + \frac{1}{\rho}\,\partial_\rho + \frac{1}{\rho^2}\,\partial_\phi^2 - \frac{s^2}{c_1^2}\right] E(\boldsymbol{\rho}) = -\frac{w(\phi)}{\rho_O}\,\delta(\rho - \rho_O) \quad \text{(A.1)}$$

where $w(\phi)$ is an arbitrary weighting function, and $\{\rho, \phi\}$ are cylindrical coordinates. Expanding $E(\boldsymbol{\rho})$ and $w(\phi)$ in terms of an angular Fourier series of the form

$$E(\boldsymbol{\rho}) = \sum_{m=-\infty}^{\infty} e_m(\rho)\exp(jm\phi),$$
$$w(\phi) = \sum_{m=-\infty}^{\infty} w_m \exp(jm\phi) \quad \text{(A.2)}$$

then results in

$$e_m(\rho) = \frac{w_m}{2\pi}\, I_m\left(\frac{s\rho_<}{c_1}\right) K_m\left(\frac{s\rho_>}{c_1}\right) + v_m K_m\left(\frac{s\rho}{c_1}\right) \quad \text{(A.3)}$$

where I_m and K_m are modified Bessel functions of order m, and where $\rho_< = \min\{\rho, \rho_O\}$ and $\rho_> = \max\{\rho, \rho_O\}$. In (A.3), the coefficients $\{v_m\}$ represent the scattered field, which contains the information on the geometry inside $\mathcal{D}_O$.

For $\boldsymbol{\rho} \in \mathcal{D}_O$, any incident field generated by sources in $\overline{\mathcal{D}}_O$ assumes the form

$$E^i(\boldsymbol{\rho}) = \sum_{m=-\infty}^{\infty} A_m I_m\left(\frac{s\rho}{c_1}\right)\exp(jm\phi). \quad \text{(A.4)}$$

Comparing (A.3) and (A.4) directly leads to the identification $w_m = 2\pi A_m / K_m(s\rho_O/c_1)$. For the *total field* in $\mathcal{D}_O$, we then have

$$E(\boldsymbol{\rho}) = \int_{-\pi}^{\pi} w(\phi_S)\, G(\boldsymbol{\rho}, \boldsymbol{\rho}_S)\, d\phi_S \quad \text{(A.5)}$$

with $G(\boldsymbol{\rho}, \boldsymbol{\rho}_S)$ defined by (2) and (3). For the *scattered field* in $\overline{\mathcal{D}}_O$, we may write

$$E^s(\boldsymbol{\rho}) = \sum_{m=-\infty}^{\infty} \exp(jm\phi)\,\frac{e_m^s(\rho_O)}{K_m\left(\dfrac{s\rho_O}{c_1}\right)}\, K_m\left(\frac{s\rho}{c_1}\right) \quad \text{(A.6)}$$

where the Fourier coefficients $\{e_m^s(\rho_O)\}$ are directly available from the scattered field on $\partial\mathcal{D}_O$. With these results, we have arrived at the desired equivalence theorems.

Appendix B
Homogeneous, Lossless Circular Cylinder

For parameter studies in the investigation of the *dynamic range* and for numerical confirmation of the *resolution analysis*, we used analytical expressions for a homogeneous,

circular cylinder, embedded in a homogeneous dielectric. In this appendix, the relevant theory is summarized.

A. Direct Problem

As a first step, we choose the line-source excitation of a homogeneous, dielectric cylinder with radius a and relative permittivity ε_{2r}, embedded in a homogeneous dielectric with relative permittivity ε_{1r}. For this equation, the second-order differential equation (2) simplifies to

$$\left[\partial_\rho^2 + \frac{1}{\rho}\,\partial_\rho + \frac{1}{\rho^2}\,\partial_\phi^2 - \frac{s^2}{c_0^2}\,\varepsilon_r(\rho)\right] G(\boldsymbol{\rho}, \boldsymbol{\rho}_P) = -\frac{1}{\rho_O}\,\delta(\rho-\rho_O)\,\delta(\phi-\phi_P) \tag{B.1}$$

where

$$\varepsilon_r(\rho) = \begin{cases} \varepsilon_{2r} & \text{for } 0<\rho<a, \\ \varepsilon_{1r} & \text{for } a<\rho<\infty. \end{cases} \tag{B.2}$$

Using separation of variables, we obtain

$$G(\boldsymbol{\rho}, \boldsymbol{\rho}_P) = \frac{1}{2\pi}\sum_{m=-\infty}^{\infty} \exp(jm[\phi-\phi_P])\, g_m(\rho, \rho_O) \tag{B.3}$$

with

$$g_m(\rho, \rho_O) = \begin{cases} I_m\left(\dfrac{s\rho_<}{c_1}\right) K_m\left(\dfrac{s\rho_>}{c_1}\right) \\ \quad + p_m K_m\left(\dfrac{s\rho_O}{c_1}\right) K_m\left(\dfrac{s\rho}{c_1}\right) & \text{for } a<\rho<\infty \\ q_m K_m\left(\dfrac{s\rho_O}{c_1}\right) I_m\left(\dfrac{s\rho}{c_2}\right) & \text{for } 0<\rho<a \end{cases} \tag{B.4}$$

where $\rho_< = \min\{\rho, \rho_O\}$ and $\rho_> = \max\{\rho, \rho_O\}$. The constants $\{p_m, q_m\}$ follow by applying the boundary conditions at the edge of the cylinder, i.e., enforcing the continuity of $g_m(\rho, \rho_O)$ and $\partial_\rho g_m(\rho, \rho_O)$ across $\rho = a$. We arrive at

$$p_m = \frac{\frac{sa}{c_1} I_{m+1}\left(\frac{sa}{c_1}\right) I_m\left(\frac{sa}{c_2}\right) - \frac{sa}{c_2} I_m\left(\frac{sa}{c_1}\right) I_{m+1}\left(\frac{sa}{c_2}\right)}{\frac{sa}{c_1} K_{m+1}\left(\frac{sa}{c_1}\right) I_m\left(\frac{sa}{c_2}\right) + \frac{sa}{c_2} K_m\left(\frac{sa}{c_1}\right) I_{m+1}\left(\frac{sa}{c_2}\right)} \tag{B.5}$$

and

$$q_m = \frac{1}{\frac{sa}{c_1} K_{m+1}\left(\frac{sa}{c_1}\right) I_m\left(\frac{sa}{c_2}\right) + \frac{sa}{c_2} K_m\left(\frac{sa}{c_1}\right) I_{m+1}\left(\frac{sa}{c_2}\right)}. \tag{B.6}$$

B. Born Approximation

Second, we consider the distorted-wave-Born approximation as formulated in Section III-A. For the *actual* configuration, we consider the homogeneous cylinder specified in Appendix B-A. For the *estimated* configuration, we consider a similar cylinder with radius $\overline{a}$ and relative permittivity $\overline{\varepsilon}_{2r}$ for $0<\rho<\overline{a}$. We are interested in evaluating the approximate field

$$G^B(\boldsymbol{\rho}_R, \boldsymbol{\rho}_S) = \overline{G}(\boldsymbol{\rho}_R, \boldsymbol{\rho}_S) - \frac{s^2}{c_0^2}\int_0^{a_>} \rho\, d\rho \int_{-\pi}^{\pi} d\phi \cdot [\varepsilon_r(\rho) - \overline{\varepsilon}_r(\rho)]\, \overline{G}(\boldsymbol{\rho}, \boldsymbol{\rho}_R)\, \overline{G}(\boldsymbol{\rho}, \boldsymbol{\rho}_S) \tag{B.7}$$

where $a_> = \max\{a, \overline{a}\}$. The integral over ϕ on the right-hand side can be evaluated by using the orthogonality of the functions $\{\exp(jm\phi)\}$:

$$\int_{-\pi}^{\pi} \overline{G}(\boldsymbol{\rho}, \boldsymbol{\rho}_R)\overline{G}(\boldsymbol{\rho}, \boldsymbol{\rho}_S)\, d\phi = \frac{1}{2\pi}\sum_{m=-\infty}^{\infty} \overline{g}_m^2(\rho, \rho_O)\exp(jm[\phi_R - \phi_S]) \tag{B.8}$$

where $\overline{g}_m(\rho, \rho_O)$ is the angular Fourier coefficient introduced in (B.3), generalized to the reference configuration. This means that we can write

$$G^B(\boldsymbol{\rho}_R, \boldsymbol{\rho}_S) = \frac{1}{2\pi}\sum_{m=-\infty}^{\infty} \exp(jm[\phi_R - \phi_S])\, g_m^B(\rho_O, \rho_O) \tag{B.9}$$

with

$$g_m^B(\rho_O, \rho_O) = \overline{g}_m(\rho_O, \rho_O) - \frac{s^2}{c_0^2}\int_0^{a_>} \rho\, d\rho \cdot [\varepsilon_r(\rho) - \overline{\varepsilon}_r(\rho)]\, \overline{g}_m^2(\rho, \rho_O). \tag{B.10}$$

$\varepsilon_r(\rho) - \overline{\varepsilon}_r(\rho)$ is a piecewise constant function. Therefore, the integral over ρ can be evaluated in closed form by breaking up the integration interval and using

$$\int z F_m^2(\gamma z)\, dz = \tfrac{1}{2}\left[z^2 F_m^2(\gamma z) + F_{m-1}(\gamma z)\, F_{m+1}(\gamma z)\right] \tag{B.11}$$

which holds for any linear combination $F_m(\gamma z) = A\, I_m(\gamma z) + B\,(-1)^m K_m(\gamma z)$. With the aid of Parseval's theorem, we then arrive at

$$\int_{-\pi}^{\pi} d\phi_R \int_{-\pi}^{\pi} d\phi_S \left|G(\boldsymbol{\rho}_R, \boldsymbol{\rho}_S) - G^B(\boldsymbol{\rho}_R, \boldsymbol{\rho}_S)\right|^2 = \sum_{m=-\infty}^{\infty} \left|g_m(\rho_O, \rho_O) - g_m^B(\rho_O, \rho_O)\right|^2. \tag{B.12}$$

With this result and a similar expression for $G(\boldsymbol{\rho}_R, \boldsymbol{\rho}_S) - \overline{G}(\boldsymbol{\rho}_R, \boldsymbol{\rho}_S)$, we are able to compute the normalized Born error as specified in Section IV-A.

C. Plane Wave Synthesis

Third, we consider the possibility of synthesizing a local plane wave inside a scattering object. Inside the cylinder, a unit-amplitude plane wave propagating in the direction $\mathbf{u}^i$ can be written as

$$E(\boldsymbol{\rho}, \phi^i) = \exp\left(-\frac{s}{c_2}\,\boldsymbol{\rho}\cdot\mathbf{u}^i\right) = \sum_{m=-\infty}^{\infty} \exp\left(jm[\phi - \phi^i]\right)(-1)^m\, I_m\left(\frac{s}{c_2}\,\rho\right). \tag{B.13}$$

The idea is to represent this plane wave for $0 < \rho < a$ as a weighted combination of Green's functions of the form

$$\int_{-\pi}^{\pi} w(\phi_S - \phi^i)\, G(\boldsymbol{\rho}, \boldsymbol{\rho}_S)\, d\phi_s = \sum_{m=-\infty}^{\infty} w_m q_m K_m\left(\frac{s}{c_1}\rho_O\right) I_m\left(\frac{s}{c_2}\rho\right) \exp\left(jm[\phi - \phi^i]\right) \tag{B.14}$$

where an angular Fourier series representation of the form (A.2) and the separation-of-variables solution (B.4) were used. The convolution form can be chosen because of the circular symmetry of the problem. Comparing (B.13) and (B.14) directly leads to the identification

$$w_m = \frac{(-1)^m}{q_m K_m\left(\frac{s}{c_1}\rho_O\right)}. \tag{B.15}$$

A similar result was also used in [27].

ACKNOWLEDGMENT

The authors would like to thank Dr. Z. Q. Peng [25] for the forward-scattering algorithm that was derived from earlier work and Dr. E. S. A. M. Lepelaars for the availability of the BFGS optimization. They would also like to thank Dr. F. E. van Vliet, E. R. Bonsen, J. H. Kop, and W. H. A. B. Janssen for their contributions to parts of this research. Finally, the authors are indebted to Dr. A. I. M. Franchois for her constructive comments on the first drafts of this article.

REFERENCES

[1] A. G. Tijhuis, *Electromagnetic Inverse Profiling: Theory and Numerical Implementation*. Utrecht, The Netherlands: VNU Science, 1987.

[2] ——, "Born-type reconstruction of material parameters of an inhomogeneous, lossy dielectric slab from reflected-field data," *Wave Motion*, vol. 11, pp. 151–173, 1989.

[3] T. M. Habashy, E. Y. Chow, and D. G. Dudley, "Profile inversion using the renormalized source-type integral equation approach," *IEEE Trans. Antennas Propagat.*, vol. 38, pp. 668–682, 1990.

[4] Y. M. Wang and W. C. Chew, "An iterative solution of two-dimensional electromagnetic inverse scattering problem," *Int. J. Imag. Syst. Technol.*, vol. 1, pp. 100–108, 1989.

[5] W. C. Chew and Y. M. Wang, "Reconstruction of two-dimensional permittivity distribution using the distorted wave Born iterative method," *IEEE Trans. Med. Imag.*, vol. 9, pp. 218–235, 1990.

[6] M. Moghaddam and W. C. Chew, "Nonlinear two-dimensional velocity profile inversion in the time domain," *IEEE Trans. Geosci. Remote Sensing*, vol. 30, pp. 147–156, Jan. 1992.

[7] N. Joachimowicz, Ch. Pichot, and J.-P. Hugonin, "Inverse scattering: An iterative numerical method for electromagnetic imaging," *IEEE Trans. Antennas Propagat.*, vol. 39, pp. 1742–1752.

[8] H. Harada, D. J. N. Wall, T. Takenaka, and M. Tanaka, "Conjugate gradient method applied to inverse scattering problem," *IEEE Trans. Antennas Propagat.*, vol. 43, pp. 784–792, 1995.

[9] A. Franchois and Ch. Pichot, "Microwave imaging—Complex permittivity reconstruction with a Levenberg–Marquardt method," *IEEE Trans. Antennas Propagat.*, vol. 45, pp. 203–215, 1997.

[10] R. F. Remis and P. M. van den Berg, "On the equivalence of the Newton–Kantorovitch and distorted Born methods," *Inv. Probl.*, vol. 16, pp. L1–L4, 2000.

[11] I. T. Rekanos, T. Y. Yioultsis, and T. D. Tsiboukis, "Inverse scattering using finite-element method and a nonlinear optimization technique," *IEEE Trans. Microw. Theory Tech.*, vol. 47, pp. 336–344, Mar. 1999.

[12] R. E. Kleinman and P. M. van den Berg, "A modified gradient method for two-dimensional problems in tomography," *J. Comput. Appl. Math.*, vol. 42, pp. 17–35, 1992.

[13] ——, "An extended range-modified gradient technique for profile inversion," *Radio Sci.*, vol. 28, pp. 377–884, 1993.

[14] P. M. van den Berg and R. E. Kleinman, "Gradient methods in inverse acoustic and electromagnetic scattering," in *Optimization with Applications*, L. T. Biegler, Ed. Berlin, Germany: Springer, 1997, pp. 173–194.

[15] R. Pierri and A. Tamburino, "On the local minima problem in conductivity imaging," *Inv. Probl.*, vol. 13, pp. 1547–1568, 1997.

[16] R. Pierri and G. Leone, "Inverse scattering of dielectric cylinders by a second-order Born approximation," *IEEE Trans. Geosci. Remote Sensing*, vol. 37, pp. 374–382, Mar. 1999.

[17] A. G. Tijhuis and F. E. van Vliet, "Practical considerations for two-dimensional velocity inversion using the distorted-wave Born iterative technique," in *Proc. 24th General Assembly of URSI*, Kyoto, Japan, August 25–September 2, 1993, p. 83.

[18] ——, "Two-dimensional Born-type velocity inversion using multiple-frequency information," in *Proc. IEEE Antennas and Propagation Society Int. Symp.*, Seattle, WA, June 19–24, 1994, pp. 2288–2291.

[19] ——, "Two-dimensional Born-type velocity inversion using multiple-frequency information," in *Proc. PIERS Symp.*, Noordwijk, The Netherlands, July 1994, 469, pp. 11–15.

[20] K. Belkebir and A. G. Tijhuis, "Using multiple frequency information in the iterative solution of a two-dimensional nonlinear inverse problem," in *Proc. PIERS Symp.*, Innsbruck, Austria, 1995, p. 353.

[21] A. Litman, D. Lesselier, and F. Santosa, "Reconstruction of a 2-D binary obstacle by controlled evolution of a level set," *Inv. Probl.*, vol. 14, pp. 685–706, 1998.

[22] W. C. Chew and J. H. Lin, "A frequency-hopping approach for microwave imaging of large inhomogeneous bodies," *IEEE Microw. Guided Wave Lett.*, vol. 15, pp. 439–441, 1995.

[23] Y. Chen, "Inverse scattering via Heisenberg's uncertainty principle," *Inv. Probl.*, vol. 13, pp. 253–282, 1997.

[24] A. G. Tijhuis and Z. Q. Peng, "Marching-on-in-frequency method for solving integral equations in transient electromagnetic scattering," *Proc. Inst. Elect. Eng. H*, vol. 138, pp. 347–355, 1991.

[25] Z. Q. Peng and A. G. Tijhuis, "Transient scattering by a lossy dielectric cylinder: Marching-on-in-frequency approach," *J. Electromagn. Waves Applicat.*, vol. 7, pp. 739–763, 1993.

[26] A. Tijhuis, K. Belkebir, P. Zwamborn, and A. Rubio Bretones, "Marching on in anything: Solving electromagnetic field equations with a varying parameter," in *Proc. Int. Conf. Electromagnetics in Advanced Applications*, Torino, Italy, 1997, pp. 175–178.

[27] A. Broquetas, J. J. Mallorquí, J. M. Rius, L. Jofre, and A. Cardama, "Active microwave sensing of highly contrasted dielectric bodies," *J. Electromagn. Waves Applicat.*, vol. 7, pp. 1439–1453, 1993.

[28] M. H. Protter, "Unique continuation for elliptic equations," *Trans. Amer. Math. Soc.*, vol. 95, pp. 81–91, 1960.

[29] A. G. Tijhuis and R. M. van der Weiden, "SEM approach to transient scattering by a lossy, radially inhomogeneous dielectric circular cylinder," *Wave Motion*, vol. 9, pp. 43–63, 1986.

[30] R. Fletcher, *Practical Methods of Optimization*, 2nd ed. Chichester, U.K.: Wiley, 1990.

Anton G. Tijhuis (M'88) was born in Oosterhout, The Netherlands, in 1952. He received the M.Sc. degree in theoretical physics from Utrecht University, Utrecht, The Netherlands, in 1976, and the Ph.D. degree (cum laude) from the Delft University of Technology, Delft, The Netherlands, in 1987.

From 1976 to 1986 and from 1986 to 1993, he has been employed as an Assistant and Associate Professor at the Laboratory of Electromagnetic Research, Faculty of Electrical Engineering, Delft University of Technology. In 1993, he was appointed full Professor of electromagnetics, Faculty of Electrical Engineering, Eindhoven University of Technology, Eindhoven, The Netherlands. He has been a Visiting Scientist with the University of Boulder, Boulder, CO, the University of Granada, Granada, Spain, the University of Tel Aviv, Tel Aviv, Israel, and with McDonnell Douglas Research Laboratories, St. Louis, MO. Since 1996, he has been a Consultant with the T.N.O. Physics and Electronics Laboratory, The Hague, The Netherlands. His research interests are the analytical, numerical, and physical aspects of the theory of electromagnetic waves. In particular, he is working on efficient techniques for the computational modeling of electromagnetic fields and their application to detection and synthesis problems from several areas of electrical engineering.

Kamal Belkebir was born in Algeria in 1966. He received the Ph.D. degree in physics from the University of Paris XI, Orsay, France in 1994.

From 1995 to 1997, he was with the University of Eindhoven, Eindhoven, The Netherlands, in a postdoctoral position. He joined the Laboratoire d'Optique Electromagnétique, University of Provence, Provence, Marseille, in 1997, and he is currently "Maître de Conférences" at the same university. His research deals with both forward and inverse scattering techniques.

Amélie C. S. Litman was born in Marseille, France, in 1972. She received the engineer degree in computer science and applied mathematics and the M.Sc. degree in applied mathematics, both from ENSIMAG, a Grande Ecole of the Institut National Polytechnique de Grenoble (INPG), Grenoble, France, in 1994. She received the Ph.D. degree in applied mathematics from the Laboratoire des Signaux et Systèmes (CNRS-Supelec), Gif-sur-Yvette, France, writing her thesis on inversion methods for the electromagnetic characterization of buried objects.

From November 1997 to June 1998, she was a Postdoctoral Researcher with Faculty of Electrical Engineering, Eindhoven University of Technology, Eindhoven, The Netherlands. Her research focused on the development of nonlinear optimization algorithms applied to inverse scattering. Since July 1998, she has been with Schlumberger, Clamart, France. Her current interests include the application of inverse problem methods and minimization techniques to oil prospection.

Bastiaan P. de Hon was born in Amstelveen, The Netherlands, in 1966. He received the M.Sc. and Ph.D. degrees in electrical engineering from the Delft University of Technology, Delft, The Netherlands, in 1991 and 1996, respectively (both cum laude).

Since 1996, he has been with the Electromagnetics Group, Faculty of Electrical Engineering, Eindhoven University, Eindhoven, The Netherlands, on a fellowship awarded by the Royal Netherlands Academy of Arts and Sciences. He has been a summer student at CERN, Geneva, Switzerland, and with Schlumberger Cambridge Research, Cambridge, U.K., and a Visiting Scientist with the University of Tel Aviv, Tel Aviv, Israel. His research interests include theoretical and numerical aspects of electromagnetic, acoustic, and elastic wave propagation. He currently focuses on issues concerning wave propagation along electromagnetic and optical waveguides, especially on fast and accurate solution techniques, the design of fault-tolerant optical fibers, time-domain spectral modes, and anisotropy.